Nuclear Engineering and Technology 53 (2021) 3112–3121

Contents lists available at ScienceDirect

Nuclear Engineering and Technology

journal homepage: www.elsevier.com/locate/net

Original Article

Studies on the effect of thermal shock on crack resistance of 20MnMoNi55 steel using compact tension specimens

K. Thamaraiselvi [a, *], S. Vishnuvardhan [a, b]

[a] Academy of Scientific and Innovative Research (AcSIR), Ghaziabad 201002, India
[b] CSIR-Structural Engineering Research Centre, Chennai 600113, India

ARTICLE INFO

Article history:
Received 15 October 2020
Received in revised form
16 February 2021
Accepted 30 March 2021
Available online 26 April 2021

Keywords:
Structural integrity
Thermal shock
Compact tension
Finite element analysis
Fracture
Crack resistance

ABSTRACT

One of the major factors affecting the life span of a Reactor Pressure Vessel (RPV) is the Pressurised Thermal Shock (PTS). PTS is a thermo-mechanical load on the RPV wall due to steep temperature gradients and structural load created by internal pressure of the fluid within the RPV. Safe operating life of a nuclear power plant is ensured by carrying out fracture analysis of the RPV against thermal shock. Carrying out fracture tests on RPV/large scale components is not always feasible. Hence, studies on laboratory level specimens are necessary to validate and supplement the prototype results. This paper aims to study the fracture behaviour of standard Compact Tension [C(T)] specimens, made of RPV steel 20MnMoNi55, subjected to thermal shock through experimental and numerical investigations. Fracture tests have been carried out on the C(T) specimens subjected to thermal transient load and tensile load to quantify the effect of thermal shock. Crack resistance curves are obtained from the fracture tests as per ASTM E1820 and compared with those obtained numerically using XFEM and a good agreement was found. A quantitative study on the crack tip plastic zone, computed using cohesive segment approach, from the numerical analyses justified the experimental crack initiation toughness.

1. Introduction

Reactor Pressure Vessel (RPV) is vulnerable to the occurrence of Pressurised Thermal Shock (PTS) during its lifetime. PTS is defined as rapid cooling of the RPV due to Emergency Core Coolant (ECC) injected into it associated with potential re-pressurization of the RPV. The combined stress from the thermo-mechanical loading can cause crack formation or in severe cases total structural failure of the pressure vessel [1]. PTS is initiated by various scenarios namely, Loss of Coolant Accidents (LOCAs), stuck open pressurizer safety or relief valve, primary to secondary leakage accidents, large secondary leaks, inadvertent actuation of high pressure injection or make-up systems and accidents resulting in cooling of the RPV from outside [2,3]. In order to ensure stability of the pressure vessel against PTS, structural integrity assessment of RPV under the event of thermal shock is crucial.

Fracture analysis of RPV forms an integral and inevitable part of structural integrity assessment of RPV against PTS. Fracture parameter has to be evaluated for postulated crack sizes by applying either Linear Elastic Fracture Mechanics (LEFM) approach or Elastic Plastic Fracture Mechanics (EPFM). The estimated fracture parameters are compared with the fracture toughness of the RPV material to predict the possible crack growth. Extensive experimental investigations on large scale components/prototypes were conducted during the period between 1975 and 1983 by the U.S. Nuclear Regulatory commission to study the implications of thermal shock on fracture behaviour [4,5]. The experiments were carried out on pressure vessels and thick walled cylinders which examined various influencing factors affecting the structural integrity of RPV during a thermal shock scenario. Large scale experiments were also conducted in countries like UK [6], Germany [3,7] and Japan [8] on cylinders and wide plates subjected to mechanical loading and thermal transient. These experiments contributed a lot to the integrity assessment methodology of RPV and provided a greater understanding of the fracture mechanism during a PTS event which is affected by a variety of influencing factors.

Carrying out large scale experiments on RPV prototype or components is not economically feasible always. Hence, to

* Corresponding author. Fatigue & Fracture Laboratory, CSIR-Structural Engineering Research Centre, Taramani, Chennai - 600113, India.
E-mail addresses: thamaraiselvi@acsir.res.in (K. Thamaraiselvi), svvardhan@serc.res.in (S. Vishnuvardhan).

https://doi.org/10.1016/j.net.2021.03.029

Nomenclature

$\dot{\Delta}_{LL}$	Rate of loading in mm/sec
Δa_{limit}	limiting crack extension capacity of a specimen
A_{pl}	plastic area under load vs. plastic LLD plot
B_N	net specimen thickness
C_1, C_2	power law constants
J_{Ic}	mode I plane strain fracture toughness
J_Q	interim value of fracture toughness
J_e	elastic component of J
J_{limit}	limiting J integral capacity of a specimen
J_p	plastic component of J
a_0	initial crack length (notch length + pre-crack)
a_k	added set of degrees of freedom
r_p	radius of plastic zone
σ_y	effective yield strength
σ_{ys}	yield strength
Δa	crack extension
a	crack size
b	uncracked ligament size
CMOD	crack mouth opening displacement
CT	compact tension
EPFM	elastic plastic fracture mechanics
LLD	load-line displacement
LOCA	loss of coolant accident
m	number of enriched nodes
N	shape function
n	total number of nodes
P	applied load
u	displacement vector
W	width of the specimen
XFEM	extended finite element method
$\psi(x)$	enrichment function

supplement large scale experiments and produce further test data for parametric study, tests on small scale laboratory specimens are performed. RPV steel is subjected to constant neutron exposure due to which the material undergoes embrittlement over its operating life. Hence, regular testing of the material's crack resistance capacity through standard specimens helps in evaluating the structural integrity assessment of RPV against thermal shock. Hodulak et al. [9] performed fracture tests on cladded plate specimens containing surface and sub-clad cracks where the specimens were subjected to thermal shock followed by bending load until cracking event was observed. The experiments proved the criticality of through-clad cracks over under-clad cracks. Chapuliot et al. [10,11] carried out experimental and numerical investigations on fracture behavior of compact tension C(T) specimens subjected to thermal shock and tensile load simultaneously. Results of the fracture tests showed that specimen with lower initial temperature failed at lesser load. Pawar et al. [12] evaluated the fracture parameter of cruciform bend specimens subjected to simultaneous application of thermal shock and bending load, numerically using finite element analysis. It was observed that when the bending stresses induced in the specimen was equal to that of an RPV under normal operating condition, the crack driving force (J-integral) was less than the fracture toughness of the material (20MnMoNi55) throughout the thermal transient. As far as the authors' knowledge, not many studies have been reported on the quantification of the effect of thermal shock on crack resistance of the RPV material.

Studies showed that the occurrence of 're-pressurization' proves to be detrimental to the integrity of RPV [13,14]. Re-pressurization indicates sudden increase in the internal pressure of the RPV due to vapourization in the overcooling process, after attaining the final temperature. A numerical analysis on RPV prototype during PTS carried out by Chen et al. [13] showed that the largest SIFs were always obtained at the critical re-pressure time.

Hence, there is a dire need to study the effect of thermal shock followed by increase in applied mechanical stress which seems to be a critical scenario. Even though Hodulak et al. [9] carried out experimental investigations in which the bending load was applied after inducing thermal shock, final temperature near the crack tip was around −80 °C whereas the average temperature of RPV at the end of cooling sequence is 30 °C.

Present work aims to study the effect of embrittlement due to thermal transient (shock) on the crack resistance curve. Experimental and numerical investigations carried out on RPV steel 20MnMoNi55 to study the impact of thermal shock on the crack resistance using Compact Tension [C(T)] specimens are presented in this paper.

2. Evaluation of chemical and mechanical properties

Chemical composition of the material 20MnMoNi55 steel is tested and the results are presented in Table 1. The chemical composition provided in Table 1 gives the average of measured values obtained from the chemical analysis of 3 specimens as per IS 8811–1998 [15]. Tension tests were carried out on round bar specimens of 6 mm gauge diameter and 30 mm gauge length, made of RPV steel 20MnMoNi55 as per ASTM E8/E8M-11 [16]. The tensile tests were carried out at different temperatures between −75 °C and 300 °C to evaluate the material properties namely yield strength, ultimate tensile strength and modulus of elasticity of the RPV material. Temperature control during the tension tests was achieved through an environmental chamber fitted to a ±500 kN universal testing machine as shown in Fig. 1. Elevated temperature was achieved using the in-built coils fitted in the environmental chamber and the sub-zero temperature was achieved by using liquid nitrogen. Three specimens were tested at each temperature. The specimens were loaded at a rate of 0.01 mm/s under actuator control until fracture. The engineering stress-strain curves of material 20MnMoNi55 steel computed from the tension tests at various temperatures is presented in Fig. 2. Thermal properties of the RPV steel (20MnMoNi55) required for the analysis have been adopted as reported by Pawar et al. [12].

Average tensile properties of the RPV steel 20MnMoNi55 are presented in Table 2. Tensile properties of the material are found to be affected by temperature where ultimate tensile strength of the material reached a minimum value at 100 °C, after which it kept increasing. However, yield strength of the material showed a steady decrease with respect to increase in temperature. Average yield strength at an elevated temperature of 300 °C is about 5% lesser than that of room temperature. At the sub-zero temperature of −75 °C, the material showed an increase of 13.2% in yield strength and 11.4% in tensile strength of those tested at room temperature. The percentage of elongation doesn't show much variation in the temperature range of 28–200 °C. Also, the percentage of elongation of the material tested at −75 °C showed loss of ductility.

Table 1
Chemical composition of 20MnMoNi55 steel.

Element	C	Si	Mn	Cr	Mo	Ni	Al	Cu
Weight (%)	0.19	0.26	1.43	0.09	0.55	0.54	0.02	0.11
Standard error (%)	0.0038	0.0044	0.0231	0.0015	0.0159	0.0084	0.0008	0.0021

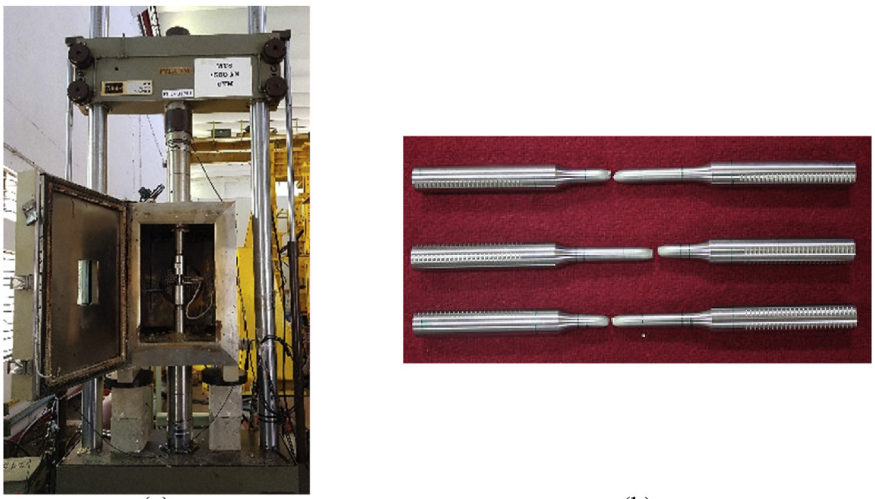

Fig. 1. (a) Tension test set-up with environmental chamber (b) Failed round bar specimens.

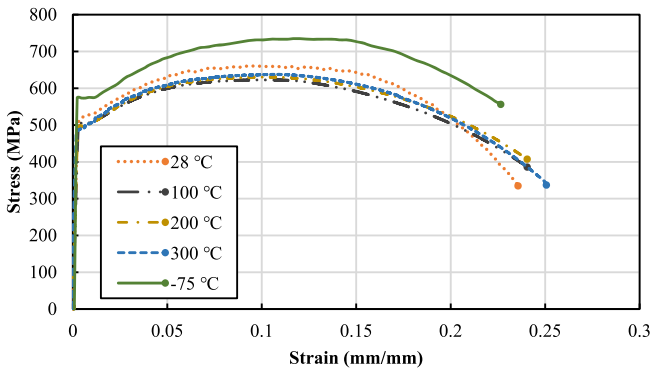

Fig. 2. Stress-strain curves for material 20MnMoNi55 steel at different temperatures.

Table 2
Average tensile properties of 20MnMoNi55 steel.

Properties	Temperature (°C)				
	−75	28	100	200	300
Yield Strength (MPa)	575	508	504	498	483
Ultimate Strength (MPa)	735	660	623	631	638
Modulus of Elasticity (GPa)	181	216	180	177	189
% elongation	22.6	23.60	24.04	24.05	25.06

3. Experimental investigation on crack resistance

To study the effect of thermal shock on fracture behavior of RPV steel, fracture tests were carried out on Compact Tension [C(T)] specimens made of 20MnMoNi55 material. In order to quantify the effect of thermal shock, the C(T) specimens were subjected to three different load cases as follows: (i) tensile load at room temperature, (ii) tensile load at elevated temperature (300 °C), which is the operating temperature of RPV and (iii) thermal transient (shock) followed by tensile load. The C(T) specimens were designed as per ASTM E1820-18 [11]. Fig. 3 shows the geometry of the C(T) specimen and details of the notch. The paper mainly focuses on the case of 're-presssurisation' phenomenon where pressure increases in the RPV due to steam after the occurrence of thermal shock. Hence, simultaneous application of thermal load and tensile load is not considered in the study. The paper studies the effect of embrittlement due to thermal transient (shock) on the crack resistance curve.

3.1. Fatigue pre-cracking

The specimens were fatigue pre-cracked using ±500 kN universal testing machine. Fatigue pre-cracking was carried out under constant amplitude sinusoidal cyclic load with a load ratio of 0.1. Maximum load was kept as 20 kN and minimum load was kept as 2 kN. Frequency of the cyclic loading was 5 Hz. The specimens were pre-cracked until the ratio of total crack length (notch length + pre-crack), a_0 to width of the specimen, W reached 0.5 ± 0.02 (deep-cracked specimens). Table 3 gives the details of the fatigue pre-cracking.

3.2. Fracture test

Fracture tests were carried out employing unloading compliance technique as per ASTM E 1820 standard [17]. The tests were conducted using ±500 kN universal testing machine under 'displacement control' where the specimens were loaded with a rate of 0.003 mm/s in a loading-unloading fashion. In order to ensure quasi-static loading, ASTM E1820 suggests that the specimens have to be loaded at a rate such that the time taken to reach the force P_m (40% of limiting force) lies between 0.3 and 3.0 min. ASTM E1921 [18] provides the time to reach P_m (t_m) or the specimen

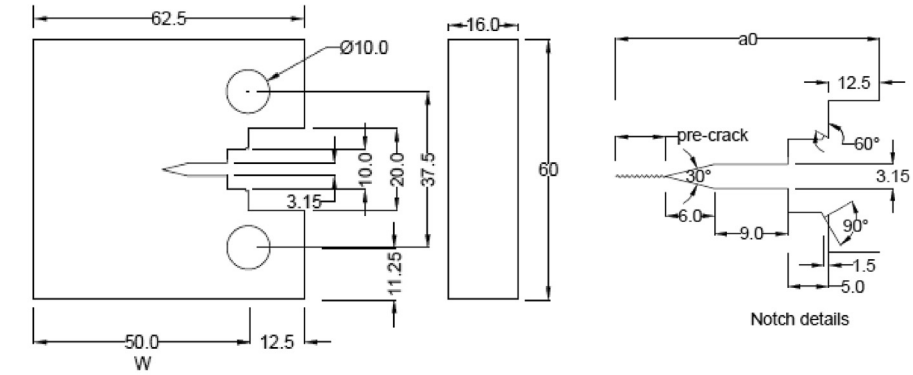

Fig. 3. Geometry of C(T) specimen and notch details.

Table 3
Details of fatigue pre-cracking.

Specimen ID	Load	Pre-crack length (mm)	No. of cycles	a_0/W
CT-RT	Tension at room temperature	6.0	19168	0.520
CT-ET	Tension at 300 °C	5.2	18253	0.504
CT-TS	Thermal shock + tension	5.0	15996	0.500

load-line displacement rate ($\dot{\Delta}_{LL}$) as a function of $\dot{K}$, W, E and σ_{YS} for different values of a/W. Based on the limiting values of $\dot{\Delta}_{LL}$, the loading rate of 0.003 mm/s was selected.

The unloading of the specimen was controlled using actuator displacement such that the unloading did not exceed 50% of the current load value. Crack opening displacement gauge of 12 mm gauge length was used for measuring the Crack Mouth Opening Displacement (CMOD). The actuator displacement, load and load-line displacement (LLD), were logged simultaneously using a data logger at a frequency of 2 Hz. The tests were carried out until a visible crack length of ~6 mm was observed (about 1/4th of the initial ligament size) which indicates the maximum crack extension capacity of the specimen as per ASTM E1820. High temperature for the specimen CT-ET was achieved using a metal heater (custom designed for CT specimen) where the temperature was sustained for a period of 5 min before application of tensile load. Two numbers of thermocouples were spot welded to the specimen as shown in Fig. 4 to measure the temperature. The test temperature was controlled within ±5 °C. The tensile load, in this case the load-line displacement, was applied after achieving the required temperature of 300 °C so that the specimen was devoid of any residual thermal stress.

Fracture test on the specimen CT-TS was carried out after inducing thermal shock in the specimen. The thermal shock was simulated by heating the specimen to 300 °C after which a thin stream of water, whose temperature was 25 °C, was applied in the notch portion until the specimen reached room temperature. It took about 370 s for the core temperature of the specimen to cool down. It should be noted that the duration of transient is similar to that of steam line break accident (300 s) and small break LOCA (388 s) as reported in the literature [19,20]. The stream of water was supplied in the notch portion in order to cool down the pre-cracked region locally in a more efficient manner.

Fig. 5 shows the load versus load-line displacement obtained for all the three specimens from the fracture tests. The maximum load sustained by the specimens (P_{max}) and the displacement required to achieve the limiting value of crack extension (LLD_{max}) are given in Table 4. It could be seen that at elevated temperature, stiffness of the material reduces and the specimen required higher load-line displacement in order for the crack to grow to a required length due to increased ductility at high temperature. It is also evident that the thermal shock induced on the specimen increases the load carrying capacity. However, thermal shock reduces the toughness of the material and hence the required crack growth was achieved at a lower load.

3.3. Estimation of J-R curve

Evolution of J-integral with stable crack growth (Δa) constitutes the crack resistance curve termed as 'J-R curve'. J-R curves are widely adopted to characterize the elastic-plastic fracture behaviour of materials. The J-R curves are being utilized to characterize the material capacity against fracture initiation, stable crack growth, and unstable tearing [21–24]. This section describes the construction of J-R curves for all the three specimens adopting 'single-specimen technique' as per ASTM E 1820.

Crack extension (Δa) is computed from the elastic compliance corresponding to each unloading path obtained from the load-CMOD data. The compliance values obtained are corrected for specimen rotation after which the corrected crack extension values are evaluated. Crack extension along with load-LLD data is used to evaluate the incremental J value. J values are computed as follows:

$$J = J_e + J_p \tag{1}$$

where J_e is the elastic component of J computed from stress intensity factor and J_p indicates the plastic component of J computed from the area under force versus load-line displacement record. The expression relating incremental value of plastic component of J with the incremental plastic area is provided in ASTM E 1820. Fig. 6 shows the J-R curves computed for all the three C(T) specimens. The crack extension-J values computed is fitted using power law as shown in equation (2).

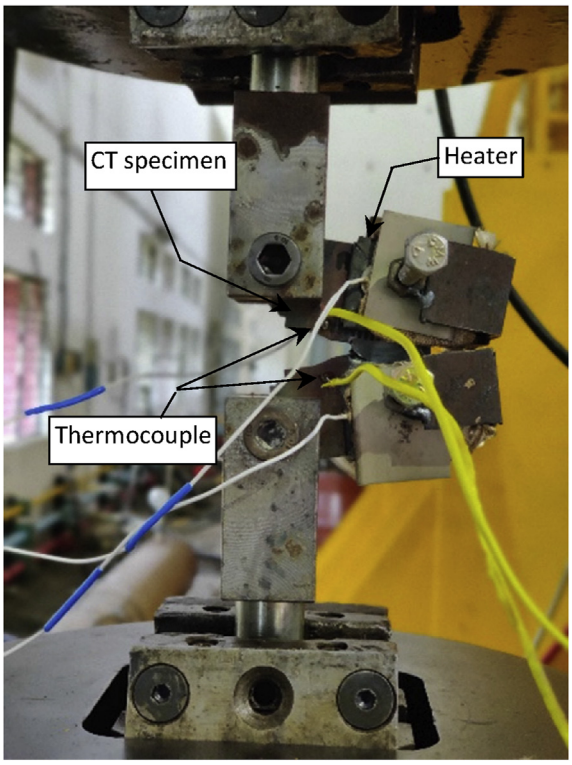

Fig. 4. Test set-up of specimen CT-ET.

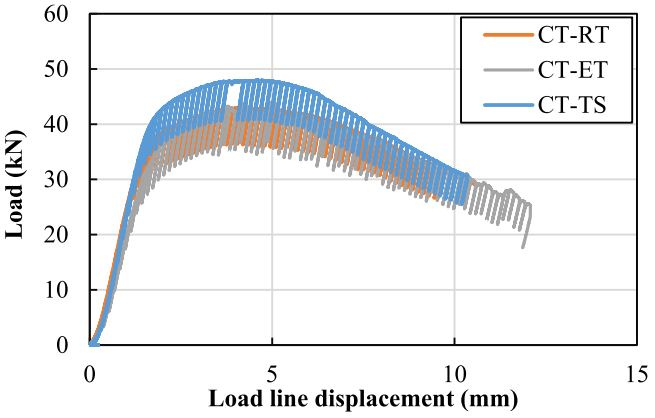

Fig. 5. Evolution of load with load-line displacement.

$$J = C_1(\Delta a)^{C_2} \tag{2}$$

C_1 and C_2 are the power law constants whose values are given in Table 4. *J-R* curve between the limiting *J* capacity of the specimen (J_{limit}) and limiting crack extension capacity of the specimen (Δa_{limit}) are taken as valid data for computation of power law curve (Table 4). As per ASTM E1820, J_{limit} and Δa_{limit} are computed as follows:

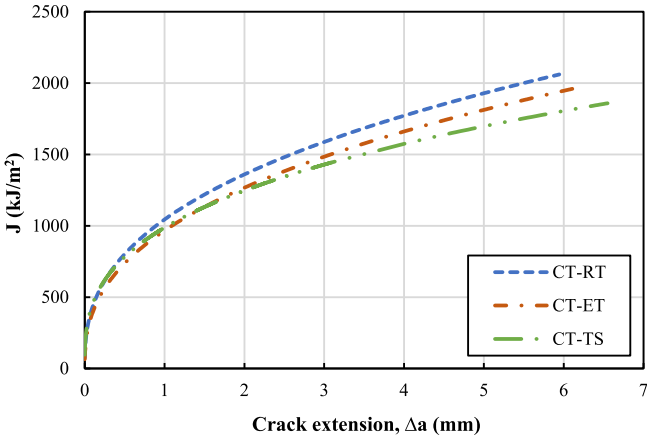

Fig. 6. *J-R* curves obtained from the fracture tests.

$$J_{limit} = b_0\sigma_y/7.5 \tag{3}$$

Where b_0 is the original remaining ligament, σ_y is the effective yield strength.

Δa_{limit} indicates the intersection of power law curve with the construction line of slope $2\sigma_y\Delta a$ at an offset distance of 1.5 mm. Toughness of a material near the onset of crack extension from a pre-existing crack is characterized by the parameter J_{Ic}, a material property, which can be computed from the *J-R* curve. As per ASTM E1820, intersection of the power law curve with an offset line at 0.2 mm gives an interim values of fracture toughness called J_Q. In order to qualify J_Q as a size independent fracture toughness of the material, the following criteria must be satisfied.

$$B, b_0 > 10\frac{J_Q}{\sigma_y} \tag{4}$$

where *B* is the thickness of the compact specimen, b_0 is the initial ligament and σ_y is the effective yield strength. Values of interim fracture toughness, J_Q computed for all the three specimens along with the validation criteria are presented in Table 4. It is evident that the thickness of the C(T) specimens do not satisfy the limiting criteria by a marginal value and hence the interim $J_Q$values obtained from the fracture tests cannot define the toughness of the material tested, i.e., the critical fracture toughness obtained is sensitive to the dimensions of the specimen.

3.4. Experimental observations

Values of J_Q obtained from the fracture tests indicate the fracture toughness is sensitive to temperature and it seems to reduce with increase in temperature. It should also be noted that despite the fact that the specimens CT-RT and CT-TS were tested at room temperatures, thermal shock reduced the initiation toughness by 3%. Reduction in fracture toughness due to thermal shock could be attributed to the quenching effect which is found to increase the brittleness of the material [25]. Even though the values of fracture toughness (J_Q) are not independent of specimen dimensions, it can be seen that they follow similar trend with increase in temperature from the results of fracture tests (J_{IC}) carried out by Bhowmik et al. [26] on 1T-C(T) specimens. Likewise, similar trend was also observed by Blauel et al. [22] in the fracture toughness values (J_{IC}) of 20MnMoNi55 steel obtained in the temperature range of 80–200 °C. Hence, it is safe to conclude that the initiation toughness values computed from the experiments predict the fracture

Table 4
Results of the fracture tests.

Specimen ID	P_{max} (kN)	LLD_{max} (mm)	Power law constants		Correlation coefficient	J_{limit} (kJ/m^2)	Δa_{limit} (mm)	Δa at the end of fracture test (mm)	J_Q (kJ/m^2)	Limiting criteria $B, b_0 > 10\frac{J_Q}{\sigma_y}$
			C_1	C_2						
CT-RT	42.54	10.65	1044.2	0.38	0.96	1872	2.76	5.947	1049.7	17.94
CT-ET	42.59	12.46	966.3	0.39	0.98	1853	2.80	6.205	966.4	17.23
CT-TS	47.26	10.35	987.32	0.34	0.96	1950	2.71	6.558	1019.5	17.43

behaviour of the material 20MnMoNi55 in the room as well as operating temperature of RPV with sufficient accuracy.

Study on the *J-R* curves, on the whole, computed from the fracture tests state that the curves are dependent on temperature where the slope and *J*-integral values reduce with increase in temperature. Crack resistance seems to reduce as the crack grows when subjected to thermal shock compared to that of specimen without prior thermal shock loading. In order to produce a crack extension of 5 mm which is about 20% of the initial ligament, the energy release rate produced for a specimen at room temperature is about 6% higher than that of elevated temperature (300 °C) and 13.7% higher than that of the specimen tested at room temperature after thermal shock. Interestingly, this reduction in J due to thermal shock is similar to that of the % reduction in *J* caused by neutron irradiation. This is conclusive from the experimental *J-R* curves on the irradiated A 533-B steel (similar in chemical composition to 20MnMoNi55 steel) wherein irradiation reduced the energy release rate of the material by ~14% for a crack extension of 5 mm when tested at a temperature of 288 °C [27]. This shows that the occurrence of thermal shock could double the loss of crack resistance capacity of the RPV steel in an irradiated state. This inturn proves that the occurrence of thermal shock could be detrimental to the structural integrity.

Reduction in crack resistance with increase in temperature could be attributed to 'dynamic strain aging'. Dynamic strain aging is a mechanism which reduces the ductility of the material due to loading of the specimen such that the interstitials diffuse and pin the mobile dislocations. The dynamic strain aging generally occurs at the upper shelf region at a particular temperature range. This mechanism is found to reduce fracture toughness of steels like SA 508 [28], 316 LN stainless steels [29] which are used in nuclear industry. Dynamic strain aging is also observed in 20MnMoNi55 steel which is found to reduce the crack resistance up to 200 °C [22,30]. The temperature range of dynamic strain aging depends on a variety of factors like rate of loading etc. Therefore further investigation is required in this front to evaluate the effects of dynamic strain aging on fracture behaviour of the material under study.

4. Numerical estimation of *J-R* curves using XFEM

This section describes the numerical investigations carried out to study the effect of thermal shock in C(T) specimens interms of crack resistance.

4.1. Extended finite element method

The extended finite element method (XFEM) is a numerical approach which is an extension of classical finite element method (FEM) wherein the solution space of differential equations is expanded using discontinuous functions [31]. In XFEM approach, the following approximation is used to compute the displacement for a point x located within the domain [32].

$$u^h(x) = u^{FE} + u^{enr} = \sum_{i=1}^{n} N_i(x)u_i + \sum_{k=1}^{m} N_k(x)\psi(x)a_k \tag{5}$$

The first term on the right hand side of Eq. (5) is the finite element approximation to determine the displacement field, while the second term is the enrichment approximation which takes into account the existence of any discontinuities. u_i is the vector of regular degrees of nodal freedom in the finite element method, n is the total number of nodes in finite element model, N_i shape function associated with node i, a_k is the added set of degrees of freedom to the standard finite element model, m is the number of

enriched nodes and $\psi(x)$ is the discontinuous enrichment function.

4.2. Construction of J-R curves

In order to evaluate the *J-R* curves numerically for each loading condition, a 3-D model of the compact specimen is constructed in Abaqus 6.18, a commercially available finite element package. *J* integral is computed using 'domain integral' method. An elasto-plastic analysis is carried out on the C(T) specimens where the stress-strain behaviour of the material is modelled using the data obtained from tension tests.

The specimens are loaded in a step by step manner using the load-line displacement data obtained from the experiments. For every increment in the load-line displacement, the corresponding crack extension obtained from the experiment is modelled as a predefined crack in the form of a 3D shell element. Enrichment radius to compute the contour integral is varied accordingly for every load step and the corresponding *J* integral is determined. The three dimensional model of C(T) specimen is constructed using linear eight noded brick elements (C3D8R) where reduced integration is employed in obtaining the solution of the governing equation. The specimen is loaded at a rate of 0.003 mm/s to enforce quasi-static behaviour. In order to compensate any localized instability that may occur during the analysis, a suitable damping factor has been employed in the step module. The displacement is applied at the loading pin/point which is kinematically coupled to the specimen where three displacement (U_x, U_y, U_z) and two rotation degrees of freedom (θ_x, θ_y) are restrained. The region around the crack plane has a mesh size of 0.55 mm constructed using sweeping technique whereas along the crack front mesh size has been restricted to 0.4 mm. J-integral is computed using domain integral technique for 20 contours around the crack plane in order to obtain the accurate value.

In order to simulate the thermal shock, the thermo-mechanical analysis is performed using Abaqus in a sequential manner, i. e., heat transfer analysis followed by static stress analysis. The heat transfer analysis is carried out to compute the spatial and temporal distribution of temperature across the specimen during the thermal transient. The temperature data during the transient, from the experiment, obtained from the thermocouples is fed as thermal boundary condition on the numerical model. The thermocouple data is the set boundary condition on one face whereas a convective heat transfer by air is set on the other face to replicate the experiment scenario. For the heat transfer analysis 8 noded convection/diffusion brick elements (DCC3D8) are employed. Fig. 7 shows the temperature data obtained from the thermocouple on the specimen CT-TS applied as the thermal boundary condition as well as

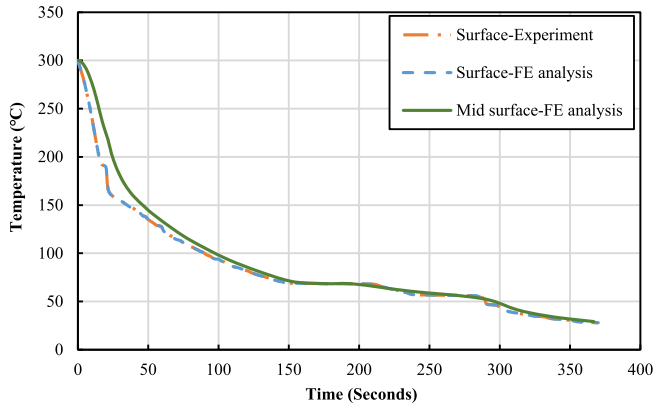

Fig. 7. Thermal transient profile.

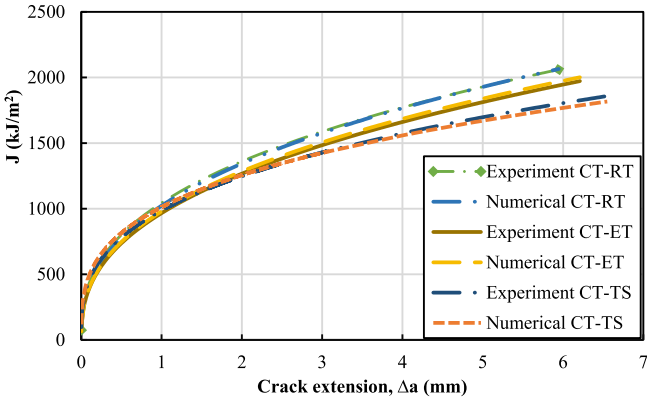

Fig. 8. Comparison of crack resistance curves.

the temperature profile obtained from the Finite Element (FE) heat transfer analysis. After simulating thermal shock, fracture analysis is performed using XFEM where crack gets opened due to tensile load. The constructed *J-R* curves are presented and discussed in the following subsection.

Plastic zone at the crack tip of the C(T) specimens has also been studied to evaluate the effect of thermal shock on crack tip constraint and the state of stress at the crack tip. Crack tip constraint can be defined as an obstruction to plastic flow which is influenced by many factors including geometrical and physical boundary conditions. Hence quantitative study of plastic zone would help us better to understand the stress triaxiality in the vicinity of the crack tip. Shape and radius of plastic zone are evaluated numerically from the results of FE analysis and analytically using the expression by Irwin and Dugdale [33].

Irwin's plastic zone radius:

$$r_p = \frac{1}{2\alpha\pi}\left[\frac{K_I}{\sigma_{ys}}\right]^2 \tag{6}$$

Dugdale's plastic zone radius:

$$r_p = \frac{\pi}{8\alpha}\left[\frac{K_I}{\sigma_{ys}}\right]^2 \tag{7}$$

where r_p is the radius of plastic zone, K_I is the mode I stress intensity factor and σ_{ys} is the yield strength. For plane stress condition, $\alpha = 1$ and for plane strain condition, $\alpha = 3$.

4.3. Results and observations of the numerical analysis

The crack resistance curves of the C(T) specimens computed from the FE analysis are shown in Fig. 8 along with those obtained from the fracture experiments. The crack resistance curve has been computed by fitting a power law to the *J-Δa* data obtained numerically using XFEM approach, mentioned in the previous section. Unlike the procedure described in ASTM E1820, the power law curve has been fitted for the complete *J-Δa* data evaluated

Table 5
Comparison of power law constants from experiment and numerical analysis.

Specimen ID	Experiment		Numerical		% difference	
	C_1	C_2	C_1	C_2	C_1	C_2
CT-RT	1044.2	0.3813	1022.8	0.394	2.1	3.3
CT-ET	966.3	0.3907	979.68	0.3912	1.38	0.12
CT-TS	987.32	0.3366	1012.4	0.3112	2.5	7.5

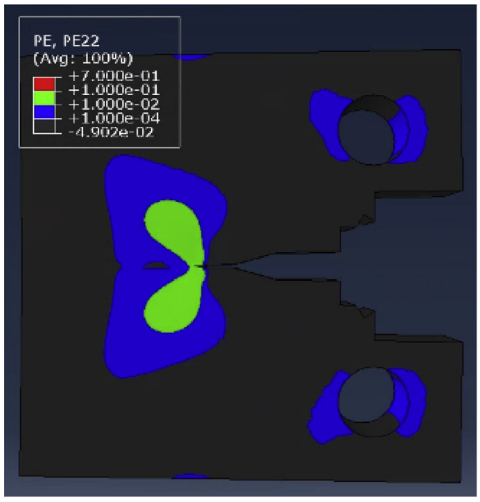

(a) LLD = 2.25 mm, $a/W = 0.500$

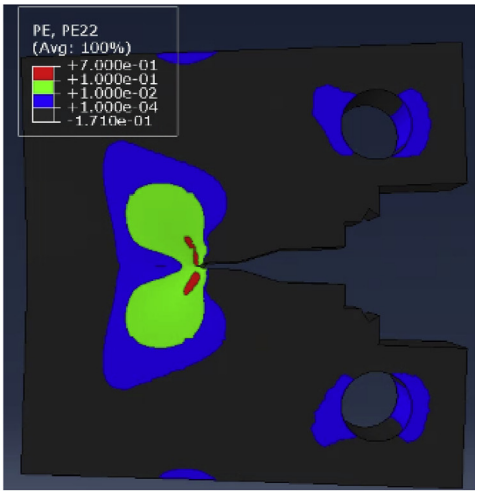

(b) LLD = 5.10 mm, $a/W = 0.518$

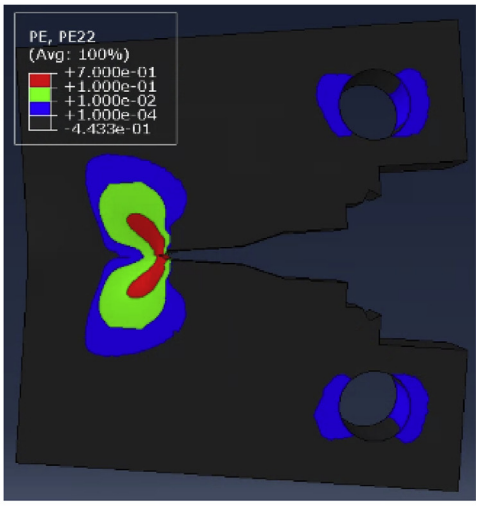

(c) LLD = 10.35 mm, $a/W = 0.631$

Fig. 9. Evolution of plastic strain in the specimen CT-TS.

numerically. It can be seen that a good agreement has been found between the experimental and numerical crack resistance curves. For the specimen tested at elevated temperature, numerically computed *J-R* curve seem to over predict the crack resistance capacity of the material by a marginal value. The power law constants of the numerically computed *J-R* curves are presented in Table 5 along with the % of variation from the experimentally computed constants. Fig. 9 shows the evolution of plastic strain in the direction of applied load (Y-direction) in the specimen CT-TS throughout the analysis. Plastic deformation is observed to be highly localized near the crack tip. It could also be observed that the region of maximum plastic strain increases with crack length.

Study on the plastic zone has been carried out at the crack extension value corresponding to the initiation toughness (J_Q), i.e., crack extension value where the 0.2% offset line intersects the power law fitted line. The crack is propagated using cohesive segment approach employing traction separation law where the damage is initiated when the maximum principal stress reaches the critical value. The damage evolution is defined based on the effective plastic displacement where the damage variable evolves in a linear fashion. Table 6 shows the radius of plastic zones computed using analytical expressions by Irwin and Dugdale (Equation (6) & (7)) and numerically from the fracture analysis using XFEM. The radius of plastic zone from the FE analysis is computed from post processing by measuring the distance between crack tip and the point along the crack front ($\theta = 0^\circ$) and perpendicular to the crack front ($\theta = 90^\circ$) up to which the stress along the direction of applied load exceeds the yield stress of the material ($\sigma_{yy} \geq \sigma_{ys}$). It can be seen from Table 6 that the radius of plastic zone computed using Irwin model predicts fairly the numerical counterpart for all three specimens along the direction perpendicular to the crack front ($\theta = 90^\circ$) both at the surface and mid-plane. The shape of plastic zone at the surface resembles the classic plane strain-plastic zone (Fig. 9). Also, maximum plastic zone size is found at the mid-section of the specimen thickness. This is in contrast to the classic 'dog-bone' shape. Similar observation has also been made by Kudari and Kodancha [34] where it was concluded that the state of stress at the surface depends mainly on the applied load.

The plastic zones obtained from the FE analysis at the surface of the three C(T) specimens have been superimposed to show the effect of plastification on the initiation toughness (Fig. 10 (a)). Fig. 10(b) shows the plastic zone overlay of all three specimens at the mid-section along the thickness. It is evident from the figure that plastic zone size of the specimens is of the following order:

$$(PZ)_{CT-RT} > (PZ)_{CT-ET} > (PZ)_{CT-TS}$$

Reduction in plastic zone at the crack tip of the specimen implies that lesser crack opening force is required. This reduction in plastification imitates the lower initiation toughness observed on the specimens CT-TS and CT-ET from the fracture tests. Eventhough the specimen tested at elevated temperature (CT-ET) has larger plastic zone size compared to the specimen CT-TS, lower initiation toughness was observed in the experiment due to dynamic strain aging mechanism. Decrease in plastic zone at the crack tip due to thermal shock implies higher triaxial stress state as compared to the specimen CT-RT. This is also confirmed by comparing the values of stress triaxiality factor at the crack tip which is found to be 0.603 for specimen CT-RT and 0.661 for specimen CT-TS.

5. Summary & conclusions

An attempt to study the effect of thermal shock on the crack resistance behaviour of RPV steel 20MnMoNi55 has been made through experimental and numerical investigations. Fracture tests

Table 6
Radius of plastic zone calculated by different methods.

Specimen ID	Irwin model		Dugdale model		FE analysis			
					($\theta = 0°$)		($\theta = 90°$)	
	Plane stress	Plane strain	Plane stress	Plane strain	Surface	Mid-plane	Surface	Mid-plane
CT-RT	4.6	1.5	11.5	3.8	2.9	5.6	4.4	4.6
CT-ET	4.4	1.5	10.9	3.6	2.8	5.2	4.2	4.5
CT-TS	4.1	1.4	10.1	3.4	2.9	5.6	4.0	4.2

*Plastic zone radius represented in 'mm'.

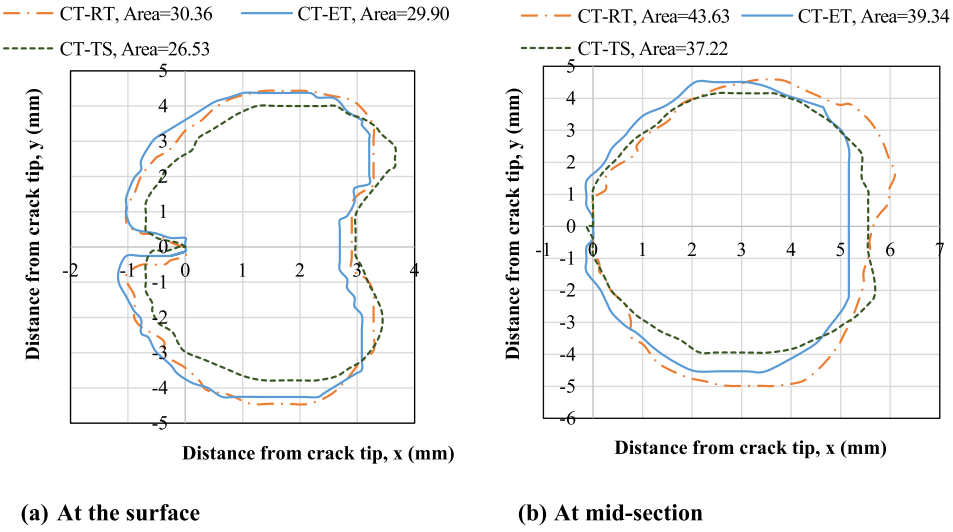

Fig. 10. Plastic zone overlay.

have been carried out on compact tension specimens under three different loading conditions namely, (i) tensile load at room temperature, (ii) tensile load at elevated temperature and (iii) thermal shock followed by tensile load at room temperature. Crack resistance curves were computed from the data obtained from the fracture tests using the procedure described in ASTM E 1820. Crack resistance curves were also computed numerically by simulating the fracture tests using extended finite element method. A quantitative study on the plastic zones at the crack tip of finite element model have also been made. The numerical analysis employing XFEM has been carried out using both predicted crack approach and cohesive segment method. To the authors' knowledge, very few works have been reported on the estimation of plastic zone size using cohesive segment method under thermal transient loading. The complete C(T) specimen has been modelled (3D) with an optimum mesh size (<2,50,000 nodes) and required level of convergence is achieved by effectively using the FE software. Following are the significant conclusions made from the study:

- Initiation toughness obtained from the fracture tests depend on the testing temperature as well as occurrence of thermal shock prior to loading. Reduction in fracture toughness after thermal shock could be attributed to increase in the brittleness of the material.
- Slope of J-R curves reduced with temperature. Reduction in crack resistance with temperature could be attributed to 'dynamic strain aging' mechanism observed in similar steel configurations. However, detailed study is required in this front to justify the behaviour at the higher temperatures.
- Specimen subjected to thermal shock prior to loading showed reduced crack resistance capacity when compared to that of specimen without thermal shock. The percentage reduction in *J* observed under thermal shock scenario is similar to that of an irradiated specimen found in the literature.
- Since RPVs are subjected to continuous neutron irradiation throughout their life and their significance in structural integrity is proved by a number of research works, it is safe to consider the combined influence of irradiation and thermal shock (gradient) on the crack resistance of the RPV material in the structural integrity assessment.
- Numerically computed *J-R* curves agreed well with that of experimental results yet there was marginal over prediction of the crack resistance capacity in the specimen tested at elevated temperature.
- Study on the plastic zones computed from the finite element analysis revealed that thermal shock reduces plastification at the crack tip. This inturn validates the reduction in initiation toughness observed from the experiment. Thus it can be concluded that the occurrence of thermal shock increases the crack tip constraint.

In order to investigate the effect of thermal shock on the crack resistance behaviour of RPV steel in a more comprehensive manner, the study has to be expanded by considering different rates of cooling.

Declaration of competing interest

The authors declare that they have no known competing

financial interests or personal relationships that could have appeared to influence the work reported in this paper.

Acknowledgements

The authors thank the Director and Advisor (Management), CSIR-SERC, Chennai for their valuable guidance, encouragement and support in the R&D activities. The assistance rendered by the technical staff of Fatigue & Fracture Laboratory, CSIR-SERC in carrying out the experiments is gratefully acknowledged.

References

[1] G. Qian, M. Niffenegger, Integrity analysis of a reactor pressure vessel subjected to pressurized thermal shocks by considering constraint effect, Eng. Fract. Mech. 112–113 (2013) 14–25, https://doi.org/10.1016/j.engfracmech.2013.09.009.
[2] International Atomic Energy Agency, Pressurized Thermal Shock in Nuclear Power Plants: Good Practices for Assessment, IAEA, Vienna, 2010.
[3] C.E. Pugh, B.R. Bass, A Review of Large-Scale Fracture Experiments Relevant to Pressure Vessel Integrity under Pressurized Thermal Shock Conditions, NUREG/CR- ORNL/TM-2000/360, TN, USA, 2000.
[4] R.D. Cheverton, J.W. Bryson, D.J. Alexander, T. Slot, Thermal-shock experiments with flawed clad cylinders, Nucl. Eng. Des. 124 (1990) 109–119, https://doi.org/10.1016/0029-5493(90)90357-4.
[5] B.R. Bass, C.E. Pugh, J. Sievers, H. Schulz, Overview of the international comparative assessment study of pressurized thermal-shock in reactor pressure vessels (RPV PTS ICAS), Int. J. Pres. Ves. Pip. 78 (2001) 197–211, https://doi.org/10.1016/S0308-0161(01)00030-8.
[6] R.C. Hurst, J.B. Wintle, B. Hemsworth, in: A.S. Rao, R.B. Duffey, R.B. Duffey, D. Elias (Eds.), NESC: the Network for Evaluating Steel Components, American Society of Mechanical Engineers, New York, 1996.
[7] L. Stumpfrock, E. Roos, H. Huber, U. Weber, Fracture mechanics investigations on cylindrical large scale specimens under thermal shock loading, Nucl. Eng. Des. 144 (1993) 31–44, https://doi.org/10.1016/0029-5493(93)90006-U.
[8] Y. Mishima, S. Ishino, M. Ishikawa, H. Okamura, G. Yagawa, T. Hidaka, T. Yamamoto, J. Sanoh, K. Koyama, M. Iida, Y. Urabe, M. Sato, M. Tomimatsu, PTS integrity study in Japan, Int. J. Pres. Ves. Pip. 58 (1994) 91–101, https://doi.org/10.1016/0308-0161(94)90012-4.
[9] L. Hodulak, J.G. Blauel, D. Siegele, B. Urich, Thermal shock experiments on cracked cladded plates, Nucl. Eng. Des. 188 (1999) 139–147, https://doi.org/10.1016/S0029-5493(99)00021-7.
[10] S. Chapuliot, M.H. Lacire, S. Marie, M. Nédélec, Thermomechanical analysis of thermal shock fracture in the brittle/ductile transition zone. Part I: description of tests, Eng. Fract. Mech. 72 (2005) 661–673, https://doi.org/10.1016/j.engfracmech.2004.07.005.
[11] M. Reytier, S. Chapuliot, S. Marie, M. Nédélec, Thermomechanical analysis of thermal shock fracture in the brittle/ductile transition zone - Part II: numerical calculations and interpretation of the test results, Eng. Fract. Mech. 73 (2006) 283–295, https://doi.org/10.1016/j.engfracmech.2004.07.016.
[12] A.K. Pawar, J. Chattopadhyay, B.K. Dutta, K.K. Vaze, Safety demonstration of RPV under PTS conditions using cruciform type specimens, in: Struct. Mech. React. Technol. SMiRT-22, IASMiRT, San Francisco, 2013, p. 406.
[13] M. Chen, F. Lu, R. Wang, A. Ren, Structural integrity assessment of reactor pressure vessel under the pressurized thermal shock loading, Nucl. Eng. Des. 272 (2014) 84–91, https://doi.org/10.1016/j.nucengdes.2015.08.020.
[14] R. Mukin, I. Clifford, H. Ferroukhi, M. Niffenegger, Pressurized thermal shock (PTS) transient scenarios screening analysis with TRACE, Int. Conf. Nucl. Eng. Proceedings, ICONE. 6A (2018), https://doi.org/10.1115/ICONE26-81749.
[15] IS: 8811, Method for Emission Spectrometric Analysis of Plain Carbon and Low Alloy Steels Point to Plane Technique, Bureau of Indian Standard, New Delhi, 1998.
[16] ASTM E8/E8M, Standard Test Methods for Tension Testing of Metallic Materials, ASTM International, Tokyo, 2011.
[17] ASTM E1820, Standard Test Method for Measurement of Fracture Toughness, ASTM International, West Conshohocken, PA, 2018.
[18] ASTM 1921, Standard Test Method for Determination of Reference Temperature , t_o , for Ferritic Steels in the Transition Range, ASTM International, West Conshohocken, PA, 2017.
[19] L.C. Wang, S.C. Jeng, N.M. Chung, Results of small break LOCA analysis for Kuosheng nuclear power plant using the RELAP5YA computer code, in: 4th Int. Top. Meet. Nucl. Therm. Hydraul. Oper. Saf., Taiwan, 1994, pp. 1–6.
[20] A.H. Khan, A.K. Ghosh, M.S. Rahman, S.M.T. Ahmed, C.L. Karmakar, An investigation on the possible radioactive contamination of environment during a steam-Line break accident in a VVER-1200 nuclear power plant, Curr. World Environ. 14 (2019) 299–311, https://doi.org/10.12944/cwe.14.2.14.
[21] X.K. Zhu, B.N. Leis, J.A. Joyce, Experimental estimation of JR curves from load-CMOD record for SE(B) specimens, J. ASTM Int. (JAI) 5 (2008) 76–91, https://doi.org/10.1007/978-981-10-6002-1_3.
[22] J.G. Blauel, L. Hodulak, T. Hollstein, B. Voss, Material characterization by J-R curves of a 20MnMoNi55 Forging, Int. J. Pres. Ves. Pip. 17 (1984) 139–162.
[23] H.S. Nam, J.S. Kim, H.W. Ryu, Y.J. Kim, J.W. Kim, Numerical ductile tearing simulation of circumferential c racked pipe tests under dynamic loading conditions, Nucl. Eng. Technol. 48 (2016) 1252–1263, https://doi.org/10.1016/j.net.2016.03.012.
[24] X. Li, Z. Ding, C. Liu, S. Bao, H. Qian, Y. Xie, Z. Gao, Effects of temperature on the local fracture toughness behavior of Chinese SA508-III welded joint, Nucl. Eng. Technol. 52 (2020) 1732–1741, https://doi.org/10.1016/j.net.2020.01.020.
[25] H.Y. Li, Y.H. Li, X.F. Wang, J.J. Liu, P.L. Xiao, Effect of quenching process on mechanical properties and ductile-brittle transition behavior of 28CrMnMoV steel, J. Cent. South Univ. 20 (2013) 1456–1461, https://doi.org/10.1007/s11771-013-1634-4.
[26] S. Bhowmik, P. Sahoo, S.K. Acharyya, S. Dhar, J. Chattopadhyay, Evaluation and effect of loss of constraint on master curve reference temperature of 20MnMoNi55 steel, Eng. Fract. Mech. 136 (2015) 142–157, https://doi.org/10.1016/j.engfracmech.2015.01.022.
[27] NUREG/CR-5493, Influence of Fluence Rate on Radiation-Induced Mechanical Property Changes in Reactor Pressure Vessel Steels, US NRC, 1990.
[28] I.S. Kim, S.S. Kang, Dynamic strain aging in SA508-class 3 pressure vessel steel, Int. J. Pres. Ves. Pip. 62 (1995) 123–129, https://doi.org/10.1016/0308-0161(95)93969-C.
[29] K.G. Samuel, O. Gossmann, H. Huthmann, Temperature dependence of fracture toughness (J-R-curves) of a modified type 316L austenitic stainless steel, Int. J. Pres. Ves. Pip. 41 (1990) 59–74, https://doi.org/10.1016/0308-0161(90)90077-U.
[30] M.S. El-Fadaly, T.A. ElSarrage, A.M. Eleiche, W. Dahl, Fracture toughness of 20MnMoNi55 steel at different temperatures as affected by room-temperature pre-deformation, J. Mater. Process. Technol. 54 (1995) 159–165, https://doi.org/10.1016/0924-0136(95)01936-7.
[31] D. Datta, Introduction to eXtended Finite Element (XFEM) Method, France, 2013. http://arxiv.org/abs/1308.5208.
[32] S. Mohammadi, Extended Finite Element Method for Fracture Analysis of Structures, Blackwell Publishing Limited, Hoboken, 2008.
[33] T.L. Anderson, Fracture Mechanics: Fundamentals and Applications, third ed., Taylor & Francis, New York, 2005 https://doi.org/10.1007/978-1-4612-1740-4. NY.
[34] S.K. Kudari, K.G. Kodancha, Effect of specimen thickness on plastic zone, 17th eur. Conf. Fract. 2008 multilevel approach to fract, Mater. Components Struct 1 (2008) 530–538.